

# Ultraviolet Jets and Bright Points in the Solar Chromosphere.

## II. Statistical Correlations

N.M. Hoekzema

Sterrekundig Instituut, Postbus 80 000, NL-3508 TA Utrecht, The Netherlands

R.J. Rutten

Sterrekundig Instituut, Postbus 80 000, NL-3508 TA Utrecht, The Netherlands

and

J.W. Cook

E.O. Hulburt Center for Space Research, Code 7668, Naval Research Laboratory,  
Washington, DC 20375-5352

Received \_\_\_\_\_; accepted \_\_\_\_\_

## ABSTRACT

We use HRTS–VI rocket observations of the solar chromosphere to search for relationships between high-Dopplershift “jets” observed in the CI lines near  $\lambda = 156$  nm and internetwork “bright points” observed in the  $\lambda = 160$  nm continuum, in sequel to the analysis by Cook et al. (1996) which failed to find a direct connection between these phenomena. We now use the same data to establish statistical correlations between CI Dopplershift and 160 nm brightness modulation in internetwork areas. These mean relations emerge only after extensive spatial averaging and have small amplitude, but are definitely significant. They show that both CI Dopplershift and 160 nm brightness participate in oscillatory behavior with three-minute periodicity and mesoscale (8 Mm wavelength) as well as small-scale (1.4 Mm wavelength) spatial patterning. We find spatial and temporal phase relations between Dopplershift and brightness that confirm that jets and bright points should not be interpreted as isolated entities. Rather, they are chromospheric manifestations, with much pattern interference, of the oscillatory acoustic shock dynamics in the internetwork which also cause Ca II  $K_{2V}$  grains. Additional small-scale modulation is present which we attribute to waves with  $f$ -mode character.

*Subject headings:* Sun: chromosphere — Sun: oscillations

## 1. INTRODUCTION

In this paper we continue the search by Cook, Rutten & Hoekzema (1996, henceforth Paper I) for relations between CI jets and 160 nm bright points in the solar chromosphere, using ultraviolet spectrograms and spectroheliograms obtained with the HRTS rocket spectrometer. Paper I failed to find a direct relationship; here, we turn to statistical correlations between jets and bright points.

Chromospheric CI jets are defined as locations where the CI resonance lines near  $\lambda = 156.1$  nm show redshifted or blueshifted emission features with apparent Dopplershift exceeding  $10 \text{ km s}^{-1}$  (Dere et al. 1983, 1986) or  $15 \text{ km s}^{-1}$  (Paper I and this paper). Their spatial extent tends to be small, often of order 1–2 arcsec. Their characteristic lifetime is about 40 s, sometimes up to 100 s. They are predominantly present in quiet-Sun internetwork areas (“cell interiors”), avoiding the chromospheric network which appears bright in the CI lines. There are more blue-shifted CI jets (“blue jets”) than redshifted ones (“red jets”).

The continuum around  $\lambda = 160$  nm presumably originates in the layers around the temperature minimum between photosphere and chromosphere, according to the VALIII standard model of the solar atmosphere (Vernazza et al. 1981). Filtergrams and spectroheliograms in this band, respectively taken with the Transition Region Camera and the HRTS slitjaw spectroheliograph, display bright network which consists of long-lived, closely packed grains, and dark internetwork areas in which more isolated bright grains appear and disappear. The latter are the 160 nm bright points discussed here. They have 50–100 K brightness temperature excess, lifetimes of about a minute and sizes of about 1 arcsec. Their spatial density of 10–30 grains per cell interior is smaller than that of CI jets; the corresponding internetwork coverages are roughly 5% and 20%, respectively (e.g., Bonnet et al. 1982; Cook et al. 1983; Foing & Bonnet 1984a, 1984b; Foing et al. 1986; paper I).

As discussed in Paper I, it has been suggested that both the internetwork CI jets and the internetwork 160 nm bright points are related to the Ca II H<sub>2V</sub> and K<sub>2V</sub> internetwork grains (Bonnet et al. 1982; Cook et al. 1983; Foing & Bonnet 1984b; Dere et al. 1986; Rutten & Uitenbroek 1991a, 1991b). The nature of the K<sub>2V</sub> grains has in the meantime been clarified, in particular through the detailed numerical simulations of Carlsson & Stein (1994). These grains are manifestations of shock formation in upward propagating acoustic waves with interference from backfalling matter from previous shocks. More detail is given in the reviews by Rutten & Uitenbroek (1991a) and Rutten (1994, 1995). The conclusion is that the quiet-sun internetwork chromosphere is pervaded by shocks to large extent, so

much that even the existence of the standard-model temperature minimum is in doubt (Carlsson & Stein 1994, 1995).

Direct connections between  $K_{2V}$  grains and 160 nm bright points or between  $K_{2V}$  grains and CI jets have never been established, for lack of the required simultaneous and co-spatial ultraviolet and Ca II data sets of sufficient quality. The only published comparison, by Martić et al. (1991), indicates qualitative spatial similarity between  $K_{2V}$  and 160 nm brightness structuring, but only after spatial smearing to 3 arcsec resolution that may largely be set by  $K_{2V}$  seeing.

Our aim in these papers is therefore to wonder whether oscillatory relationships may be found between 160 nm bright points and CI jets alone, possibly with phase delays as suggested by Rutten & Uitenbroek (1991b). Paper I searched for direct one-to-one relationships without finding any. In this paper we turn to statistical analysis of the same HRTS data set, correlating Dopplershift and brightness at all magnitudes rather than only the extreme excursions, and averaging the data spatially in order to suppress noise. Small-amplitude but significant relationships then emerge.

## 2. INPUT DATA

The observations used for this study are the same as in Paper I (Cook et al. 1996). They were obtained with the HRTS–VI rocket flight on 1988 November 20 and are briefly summarized here. Further detail is given in Paper I.

The 160 nm continuum data consist of seven spectroheliograms taken in an 1 nm passband centered at  $\lambda = 160$  nm. They were exposed during 7.2 s at roughly 25 s intervals, spanning a duration of 160 s. Meanwhile, the slit of the HRTS spectrograph was stepped across the field so that each pixel of the seven heliograms was sampled once for CI Dopplershift during this period.

Following Paper I, we limit the analysis to a  $150 \times 87$  arcsec subfield that is relatively free of blemishes and covers the seven 160 nm heliograms. It is shown in Fig. 1 (CI Dopplershift) and Fig. 2 (160 nm brightness). The pixels are  $0.5 \times 0.5$  arcsec. The spatial resolution is about 1 arcsec, as is the precision of the alignment between the CI map and the 160 nm heliograms. The scanning for the Dopplershift map (upper panel of Fig. 1) was sequential with the slit oriented along rows; the top row was measured 160 s after the bottom row. The bottom and top parts were scanned with 2 arcsec slit steps; the middle part in 1 arcsec steps.

The lower panel of Fig. 1 is an enlargement of the center part of the subfield. The

preponderance of blue jets over red jets is evident. Most jets represent peaks: they lie in wider areas with smaller Dopplershift of the same sign (blue within green, red within yellow). This suggests an oscillatory pattern of which the jets mark wave extrema, rather than a flat background from which jets arise as isolated features.

The observed 160 nm brightness values were converted into brightness temperatures  $T_b$  by assuming that the spatially and temporally averaged mean intensity equals the Planck function for  $T = 4300$  K, representative of the VALIII temperature minimum. This choice is somewhat arbitrary. The resulting brightness temperatures seem slightly lower and slightly higher, respectively, than the comparable scans in Cook et al. (1983) and Foing et al. (1986). However, our discussions below concern only differential  $T_b$  changes.

The top panel in Fig. 2 shows the selected subfield from the first of the seven heliograms. It displays the network as bright extended patches while the internetwork is filled with grainy brightness structures at various scales. Some of the fine-scale variation is due to film grain. The second panel, the same as Fig. 2 of Paper I, shows the average of the seven heliograms. The averaging reduces the film grain noise as well as the internetwork brightness variation which varies considerably between heliograms. It enhances the network–internetwork contrast since the network is relatively stable. The third panel shows reverse patterning by displaying the rms brightness temperature variation  $\sigma T_b$  per pixel over the seven heliograms. In this representation the more stable network tends to be dark, while the internetwork regions display patchy clustering with blobs of 4–10 arcsec, corresponding to the “8 Mm wavelength scale” discussed by Foing & Bonnet (1984a), Foing et al. (1986), Martić & Damé (1989) and Cook & Ewing (1991). It is enhanced in the bottom panel of Fig. 2 by spatial smoothing plus coarse brightness binning. The third panel also shows substantial brightness variation at much smaller spatial scales, close to the 1 arcsec resolution limit and corresponding to the 1.4 – 3 Mm characteristic bright point separation noted by Foing & Bonnet (1984a, 1984b) and Foing et al. (1986).

The bottom panel of Fig. 2 displays the network mask to restrict the analysis below to internetwork alone. It cuts out all all pixels in the second panel that are over 10% brighter than the spatial mean. These areas are colored grey in Fig. 1.

The color black in Fig. 1 marks special locations where the HRTS data-analysis algorithm was not able to assign a Dopplershift to a CI emission feature by taking its first moment. For extended black areas (upper panel), such failure is generally due to lack of signal. Most of the small-scale black areas in the lower panel lack well-defined peaks in their CI profile (Paper I). These tend to lie within blue areas, suggesting that their non-measurability goes together with blue-like properties. Such black-near-blue pixels are treated below as a special Dopplershift class, and indeed turn out to behave generally as

blue pixels—or even bluer than blue ones. With this in mind, the Dopplershift map also indicates split-scale patterning reminiscent of the 8 – 1.4 Mm spatial dichotomy of Foing & Bonnet (1984a).

### 3. STATISTICAL CORRELATIONS

When searching for solar relationships between brightness and intensity, one tends to either analyze data in the space-time domain, searching for coincidence between characteristic structures or events, or to turn to Fourier methods to disentangle multiple oscillatory components. In Paper I the first approach was tried by defining bright points and blue jets as specific entities. The logical alternative is to try the Fourier domain. However, each location in the CI Dopplershift map has been measured only once, whereas the seven 160 nm heliograms represent coarse temporal sampling of brief duration (160 s). Thus, Fourier analysis is not feasible on these rocket data and has to await longer-duration SUMER sequences.

However, a third tack is feasible thanks to the absence of atmospheric seeing in space. The CI Dopplershift map and the 160 nm heliograms are spatially aligned to about the resolution limit. Since there are no larger-scale time-dependent “rubber sheet” geometrical deformations as in groundbased observing, pixel-by-pixel comparisons may be averaged to diminish the confusion that may arise from instrumental noise and solar interferences. Such selective averaging constitutes our approach below.

#### 3.1. Distributions

Figure 3 details the relationship between time-averaged 160 nm brightness  $T_b$  and temporal variability  $\sigma T_b$  that is seen qualitatively by comparing the second and third panels of Fig. 2. The scatter cloud has upward and rightward tails made up by dark to medium bright but variable internetwork pixels and by very bright but time-constant network elements, respectively. The mean curve in the bottom panel has a slope change at the network cutoff value. The righthand end at  $\sigma T_b \approx 10$  K is about equal to the lower boundary of the scatter cloud and marks the rms variation of the brightest network grains. Since these are stable, the value indicates the noise level due to emulsion grain. The 10 K value (min-max excursions  $2\sqrt{2}\sigma T_b \approx 30$  K) is similar to the emulsion noise in other HRTS results and the TRC data of Foing & Bonnet (1984b). The largest values of  $\sigma T_b$  lie in the internetwork domain left of the dividing line. They reach up to  $\sigma T_b \approx 60$  K or about 170 K brightening. The mean internetwork variation  $\sigma T_b \approx 20$  K is twice the noise.

Figure 4 shows the same quantities plotted against CI Dopplershift and excluding network. The two scatter plots do not show correlation, but mean relationships appear in the lower panels by averaging per Dopplershift bin. Their amplitudes are much smaller than the spread in the upper panels (note the vertical scale expansions), but the symmetry of the two curves and their roughly parabolic shape suggest that, on the average, 160 nm brightness and CI Dopplershift are related to each other. These average correlations could be partially due to non-excluded network pixels, but they remain present in tests (not shown) with lower-temperature network cutoffs. The time-delay statistics discussed below add significance to their interpretation as an internetwork characteristic.

Figure 5 shows Dopplershift statistics. The solid curve in both panels specifies the internetwork surface fractions of the color-coded areas in Fig. 1. It quantifies that blue jets ( $\Delta\lambda_D > 15 \text{ km s}^{-1}$ ) are more numerous than red jets ( $\Delta\lambda_D < -15 \text{ km s}^{-1}$ ) as noted by Dere et al. (1983, 1986) and also seen in Fig. 4 of Paper I.

The dotted curves similarly specify Dopplershift distributions, but only for “bright points” by spatial averaging over those pixels that show large temporal 160 nm brightness variation. The lefthand panel specifies the Dopplershift distribution of pixels with  $32 < \sigma T_b < 43 \text{ K}$ . More precisely, we selected the pixels with  $90 < 2\sqrt{2}\sigma T_b < 120 \text{ K}$ , corresponding to a statistical min–max change in this range; this definition was used rather than the actual measured difference  $T_b^{\text{max}} - T_b^{\text{min}}$  per pixel in order to reduce noise, particularly from darkenings when the spectrograph slit passed over the pixel. This selection makes up 4% of the total area (non-black and non-grey in Fig. 1). The righthand panel is for pixels with  $\sigma T_b > 43 \text{ K}$ , with a filling factor of only 0.4%. The squares result when black pixels that are adjacent to blue jets are included in the blue-jet bin.

The dotted distribution at left is similar to the general distribution, except for the two extreme Dopplershift bins which are favored by large-variability pixels. These bins show substantial enhancement at right, especially when the black-near-blue pixels are added to the blue-jet bin (square at top right). Both extreme Dopplershift bins then contain twice the fraction of large-variability pixels that the general distribution has, at the cost of low-Dopplershift contributions. Thus, pixels with excessive 160 nm brightness variation lie preferentially at CI jet sites.

Note that even if all extreme 160 nm brightenings actually coincide with a CI jet location (simultaneously or at some phase lag), these distributions would not reach unity because the Dopplershift of each location was sampled only once. If all excessive  $\Delta T_b$  locations mark blue-jet locations at some phase delay, the single spectrograph scan would have missed many of the latter by sampling other CI Dopplershift phases.

### 3.2. Temporal relations

Having found that, statistically, excess 160 nm variability correlates with excess CI Dopplershift, we now turn to the question of temporal phase delay. Our tactic is again to spatially average over bins of pixels with specific properties. Since the CI Dopplershift was measured only once per pixel, simultaneously along rows in Fig. 1 and sequentially from bottom to top, we use the seven 160 nm heliograms to provide temporal variations with phase fixed to the moment of Dopplershift sampling. We have combined narrow strips from the heliograms into a single map that shows the 160 nm brightness per location within 15 s of the moment  $t = t_0$  of its Dopplershift sampling. Similarly constructed maps specify 160 nm intensity per pixel at times 26, 52, 78, 104 and 130 s before and after the corresponding CI Dopplershift was measured. From these, we measured 160 nm brightness behavior per pixel as a function of positive or negative time lag with regards to the Dopplershift sampling. The time delay axis then covers 260 s duration. Pixels at the top of the CI map in Fig. 1 furnish 130 s of 160 nm brightness history, while the brightness of pixels at the bottom of the CI map are followed for 130 s after their Dopplershift sampling. The results are shown in Figs. 6–8.

In Fig. 6 the time-delay bins are further split according to CI Dopplershift. The curves show the spatial average of the 160 nm brightness evolution  $\Delta T_b(t) \equiv T_b(t) - T_b$  of all pixels for which a given Dopplershift was measured when that pixel was sampled. Thus, the upper curve shows the brightness prior to, at, and after the moment of Dopplershift sampling, averaged over all pixels at which a red jet was measured. The curve displays small-amplitude but significant modulation, far larger than the variance around the mean curve. The modulation implies that pixels with a red jet at  $t = t_0$  are, on average, slightly brighter two minutes before the jet sampling, darker half a minute before the jet, brighter a minute after, and then darken again. In contrast, blue jets (lowest curve) produce reversed time modulation, with average brightening during the minute up to the jet, and darkening for about a minute after the jet. This agrees with the visual correlation noted from Fig. 3 in Paper I, in which blue jets seem to favor dark regions of the 160 nm heliograms at a phase lag of about half a minute.

Together, the red-jet and blue-jet curves suggest the presence of wave-like modulation with about three-minute periodicity and 180 degrees phase shift between red and blue. The intermediate curves (Y, W and G for yellow, white and green Dopplershift bins, corresponding with the color coding of Fig. 1) display corresponding phase patterns but decreasing amplitude for decreasing Dopplershift size. This reduction may be partially due to phase mixing, since measuring small Dopplershift from a pixel that takes part in a regular Dopplershift oscillation does not discriminate between the rising and descending branches.

Only the extreme Dopplershift values sample the phase of such oscillations precisely.

The bottom panel of Fig. 6 shows similar time-delay modulation statistics for “black-near-blue” pixels. The blue jet curve from the upper panel is added for reference (dashed). The solid curve displays similar three-minute modulation with similar phase at somewhat larger amplitude. Thus, these locations with complex CI profiles seem to behave as blue (or bluer than blue) jets.

These results may also be cast in the form of Fig. 5 by plotting time-delay statistics for only those 160 nm pixels that show excessive brightness variations. This is done in Fig. 7, showing that 160 nm bright points adhere to the modulations seen in Fig. 6. The solid curve in the bottom panel of Fig. 7 indicates that red jets are never exceptionally bright at the very moment, but that about 100 s earlier and 50 s later, their locations make up about 40% of all 160 nm pixels that show large temporary brightening at these time delays from the Dopplershift measurement. Reversely, about half of the extreme 160 nm brightenings which occur 50 s before or 100 s after the Dopplershift was sampled had blue-jet or black-near-blue Dopplershift at the moment of sampling, twice to three times the normal surface fraction covered by these Dopplershifts (solid distribution in Fig. 5).

### 3.3. Spatial relations

The increase of modulation amplitude from blue-jet pixels to black pixels in Fig. 6 indicates that the centers of blue jet areas may possess the largest average brightness modulation. We have therefore split the jet areas geometrically into jet centers, defined as jet pixels that are fully surrounded by other jet pixels ( $\Delta\lambda_D > 15 \text{ km s}^{-1}$ ), and the remaining jet areas. This split produces the average relations in Fig. 8. Spatial time-delay averaging over blue jet-center pixels alone (the top curve in the upper-left panel) indeed produces appreciably larger three-minute modulation than for the remaining blue jet pixels (second curve, modulation amplitude similar to the overall blue-jet curve in Fig. 6). For red jets (right-hand panels) the concentration of modulation amplitude towards the jet center is less outspoken.

The bottom curves in the top panels and the bottom panels of Fig. 8 concern jet perimeters, being the first pixels outside a jet area. In the upper panels, these behave qualitatively as the non-center jet pixels (middle curves). In the lower panels, the perimeter-pixel averaging has been split again, now between relatively high Dopplershift (dashed) and low Dopplershift (dot-dashed) areas, with the complete sample shown for reference (thin solid curve). The righthand panel has larger variances due to the smaller number of red-jet pixels. The lefthand panel shows significant differences in both average

phase and average modulation between low and high Dopplershift perimeters. The averaged low-Dopplershift perimeter modulation varies in counterphase to the averaged blue-jet center modulation, whereas the averaged high-Dopplershift modulation appears to be in phase. The red-jet panel, though noisy, suggests similar phase behavior. Thus, the averaged correlation between brightness modulation and Dopplershift decays fast with separation from jet center, especially for blue jets. For these, the modulation flips phase already one 0.5 arcsec pixel outside the jet when the Dopplershift there is small.

The spatial decay of the averaged correlations around jet areas is studied further in Fig. 9. The seven-heliogram averaged brightness temperature per pixel  $T_b$  and the averaged variability  $\sigma T_b$  that were binned for Dopplershift in Fig. 4 are now binned for jet geometry. The upper panels show that on average, both blue jets (triangles) and red jets (squares) are darker than their surroundings but show larger brightness variability at 160 nm. The lefthand panel indicates a significant difference between red and blue jets, the latter being darker.

The lower panels of Fig. 9 result from averaging exclusively over areas in and around jets which contain jet centers. The variances are therefore larger than in the top panels, but the correlations are nevertheless well-defined which implies that selecting these jets enhances the selection of specific horizontal patterning. The latter differs strikingly from the correlations in the top panels, particularly for the  $\sigma T_b$  panel at right in which the two curves display opposite behavior with enhanced variability close to blue jets and reduced variability near red jets. The split between the curves starts already within the jets ( $\Delta r = -1$ ) and extends to  $\Delta r \approx 3$  over 4 pixels, corresponding to 2–3 arcsec spatial distance (pixel diameters being 0.5–0.7 arcsec depending on direction).

The pattern suggests spatial periodicity with this wavelength. Such small-scale periodicity may, if present, show up also in the images themselves. Tests for 2–3 arcsec spatial periodicity in the 160 nm heliograms are hampered by the emulsion graininess, but the elaborate analysis of Foing & Bonnet (1984a) gave evidence for 1.4 Mm (2 arcsec) preferred bright-point separation. A similar test for spatial periodicity in the CI Dopplershift map is shown in Fig. 10. It results from an analysis in which sites with extreme Dopplershifts were selected that are well apart. Pixel rings were cast around them with increasing radius; for each, the surface fraction occupied by pixels with Dopplershift  $|\Delta\lambda_D| > 21 \text{ km s}^{-1}$  of the same sign was measured. This was done for two vertically narrow subfields, the first being the one shown in the lower panel of Fig. 1, the other one outside the area shown in the upper panel (and without 160 nm coverage). The resulting curves in Fig. 10 differ appreciably between the two subfields, by more than the Poisson variance estimates. Nevertheless, the curves show humps that indicate a preference for jet repetition at 3–4

pixel separation (corresponding to 1.8–2.4 arcsec). This result agrees with the impression from the lower panel of Fig. 1 that many jets possess split centers.

#### 4. DISCUSSION

The diagrams above show relationships between C I Dopplershift and 160 nm brightness that are statistically significant. The key features are the skewedness of the bright-point distribution with Dopplershift (Fig. 5, the opposite red and blue modulations in Fig. 6, the preference of the largest brightness changes in Fig. 7 to occur at specific phases of the Dopplershift modulation, the spatial scalings in Figs. 8–10, and the spatially-averaged morphological differences between red and blue jets in Figs. 8–9. Altogether, they indicate the existence of oscillatory phenomena in internetwork regions, with about three-minute temporal periodicity and 2–3 arcsec horizontal scaling, in which both signals participate with definite phase relationships between them.

Obviously, these modulations are reminiscent of the chromospheric three-minute oscillation known from the Ca II H&K lines and other diagnostics, also a small-scale internetwork phenomenon (see reviews by Rutten & Uitenbroek 1991a; Rutten 1994, 1995). However, while significant within their statistical variances, the modulations do not imply one-to-one feature-by-feature relationships as searched for in Paper I. The bottom panel of Fig. 7 shows that half of the 160 nm brightenings precede or follow blue jets or red jets at specific time lags, but that plot holds only for the most exceptional brightenings. Their internetwork area filling factor at any one moment is less than 0.5%. The 45–60 K brightenings in the upper panel make up only 1–2% of the area; for them the jet-correlated modulation drops already to about 20%.

Our finding of statistical correlations at small amplitude suggests that either only a few exceptional bright points and jets alternate in such phase-delay patterns, or that more global oscillatory relationships are heavily masked by other phenomena. We have tested the first possibility by replotting the distributions in Figs. 6 and 7 after deleting the pixels with the largest  $\Delta T_b$ , with various cutoffs. We found that the correlations in the upper panel of Fig. 7 loose amplitude for lower cutoff but remain significantly present, while the modulations in Fig. 6 diminish only marginally. These tests indicate that the brightest points (excessive  $\Delta T_b$ ) mark extremes of modulations that are present also more generally, as is also indicated by the small variances in Fig. 6. This implies considerable masking by measurement noise and solar interference.

#### 4.1. Noise and interference

The righthand end of the mean curve in the second panel of Fig. 3 indicates a noise limit of about  $\sigma T_b \approx 10$  K or excursions of order 30 K. This noise is mostly due from emulsion grain. Its contribution is largest at small scales so that our spatial averaging reduces its effect. The CI Dopplershift measurement is less sensitive to film grain because it uses the full line profile.

Other instrumental noise comes from variations in heliogram image quality. The spectrograph slit is vaguely seen in some of them, for which we have corrected implicitly by estimating min–max brightness temperature variations from the rms variations instead of taking the measured excursions. The heliograms also differ in quality; in particular, the one taken 199 s after launch appears somewhat sharper than the others (Fig. 3 of Paper I). Presumably, pointing instabilities or rocket vibrations have affected the latter in varying degree.

The lefthand end of the mean curve in the second panel of Fig. 3 shows an average internetwork increase of the brightness variability  $\sigma T_b$  of order 10 K over the small-scale noise limit indicated by the righthand end. The few-degree amplitudes of the averaged modulations seen in Fig. 6 and Fig. 8 are tiny with respect to the temporal and spatial variations per pixel, but they are substantial within this averaged variability and clearly significant within their variances. Thus, our spatial averaging over specific phase delay bins and jet-geometry bins in these figures brings out significant average correlations that otherwise drown in noise. The combination of small amplitudes and small variances suggests that most noise actually results from interference between intrinsic solar variations.

Considerable solar interference is undoubtedly present. If our relationships follow from regular oscillatory behavior such as the chromospheric three-minute oscillation, phase mixing occurs because we do not Fourier-decompose the different temporal and spatial frequencies in our plots. The so-called chromospheric three-minute oscillation is a broad-band phenomenon largely made up by extended  $(k, \omega)$  power ridges (e.g., Deubner et al. 1994, Hofmann et al. 1995). Such wide temporal and spatial bandwidths dilute the amplitudes of the temporal modulations for the phase-fixed extreme Dopplershift bins in Figs. 6–8, and of the spatial modulations seen in Figs. 9–10. In addition, the larger-scale brightness modulation with about 3–5 min periodicity found by Cook & Ewing (1991) by concentrating on the background 160 nm continuum that underlies the bright points indicates a substantial contribution from the five-minute  $p$ -modes.

Solar interference may also be generated by the juxtaposition of non-sinusoidal wave modes. The disparity between blue jet geometry and red jet geometry in Figs. 8 and 9

indicates more complex wave forms, as does the asymmetry of the distributions in Fig. 5. This is again reminiscent of the formation of Ca II  $K_{2V}$  grains, in which vertical interference between upwards traveling shocks and post-shock downfall causes large disparity between  $K_{2V}$  and  $K_{2R}$  behavior.

Finally, it is possible that CI Dopplershift and 160 nm brightness are related with longer phase delays than our total data duration, or with additional phase scrambling from varying delays. Both occur in the formation of the Ca II  $K_{2V}$  grains for which there is considerable delay between the driving Doppler excursions in the photosphere and much variation in the subsequent chromospheric grain patterns (Carlsson & Stein 1994; cf. Rutten 1995).

## 4.2. CI line formation

So far, we have restricted ourselves to the observational terminology of “Dopplershift” and “brightness” rather than velocity and temperature. Interpretation requires discussion in the latter terms, and therefore a closer look at CI line formation. In their initial paper on jets, Dere et al. (1983) show a plot of CI line profiles. These display distinctive large-amplitude peaks that are shifted considerably from the rest wavelengths and have more or less gaussian shapes, apart from the multiplet blending. Dere et al. (1983) argued that the observed absence of self-reversals in the peaks permits optically thin interpretation, although the CI lines are optically thick in the standard modeling by Shine et al. (1978). The latter authors display OSO 8 data with self-reversed CI line cores possessing central dips, especially for the multiplet near  $\lambda = 165.7$  nm but also for the stronger two of the three distinct lines made up by the five multiplet components near  $\lambda = 156.1$  nm. In addition, all lines reach about the same peak intensity. In contrast, the blue-jet peaks in Fig. 3 of Dere et al. (1983) reach much higher intensities than the background non-jet profiles shown in the same figure, and display increasing peak intensity and increasing Dopplershift for larger line strength. This behavior indicates lack of the saturation shown by the three background profiles. Thus, at first sight the blue-jet peaks indeed behave as optically thin high-intensity features.

Optically-thin interpretation permits direct conversion of CI peak Dopplershifts into vertical velocities. The blue-jet values of  $v \approx 10 - 20$  km s<sup>-1</sup> led Dere et al. (1983) to tentatively identify jets with spicules, the more so since no other EUV spicule candidate was found. Dere et al. (1986) did no longer suggest spicules, but suggested a phenomenon related to 160 nm bright points and internetwork Ca II  $K_{2V}$  grains.

Our result that the CI lines indeed display internetwork dynamics reminiscent of  $K_{2V}$

grain formation requires comparison with the formation of Ca II H & K. The CI 156 nm lines are 1–2 orders of magnitude more opaque than Ca II H & K. The source function plot in Fig. 4 of Shine et al. (1978) shows thermalization to appreciably larger height than in comparable Ca II K modeling, producing high twin peaks in the resulting line profiles (their Fig. 5). This implies that the Dopplershifts of the observed CI peaks may not simply encode motions in optically-thin fashion, and suggests a closer look at Ca II K<sub>2V</sub> peak formation.

In the case of the H & K lines, the classical explanation of line-core emission features as source function coupling to the chromospheric temperature rise has, for the internetwork regime, been replaced by the dynamical modeling of Carlsson & Stein (1994). They even doubt the existence of a mean internetwork chromospheric temperature rise in the layers sampled by Ca II K (Carlsson & Stein 1995). Instead, the internetwork chromosphere is filled with upward-traveling shocks of which the ultraviolet emission is erroneously interpreted in empirical VALIII-style modeling as mean chromospheric temperature rise. The bright H<sub>2V</sub> grains arise from vertical patterning of upcoming fresh shocks and backfalling matter behind preceding shocks, with much interference and temporal variation. The patterns are set by the vertical motions of the underlying photosphere, but with 5–15 min delays between the photospheric pistoning and the resulting Ca II response.

The parameter diagrams in Figs. 8–12 of Carlsson & Stein (1994) are of particular interest here because these detail H<sub>2V</sub> grain formation in the form of breakdown snapshots. Figs. 10–12 show bright H<sub>2V</sub> peaks at apparent Dopplershift  $\Delta\lambda_D \approx 10 \text{ km s}^{-1}$  that is *twice* the actual gas velocity at the height of peak formation. This large skewing results from the steep velocity gradients across the shocks higher up. Thus, at the height of K<sub>2V</sub> intensity formation, shock dynamics not only causes the striking prominence of H<sub>2V</sub> peaks over H<sub>2R</sub> peaks, but also produces doubling of the apparent peak Dopplershift over the intrinsic local Dopplershift.

How do the CI peaks measured as chromospheric jets with HRTS compare to the Ca II H<sub>2V</sub> peaks in the Carlsson-Stein simulation? The blueshifted CI peaks in Fig. 3 of Dere et al. (1983) are qualitatively similar to the H<sub>2V</sub> peaks in Figs. 11 and 12 of Carlsson & Stein (1994). The CI lines differ in lacking a much wider absorption profile as shown by Ca II H, but this difference is due to the formation of the background continuum. The peaks have similar lifetimes, similar 2–4 min periodicity, are similarly asymmetric with longer tails towards line center, vary similarly in apparent Dopplershift and vary strongly in amplitude in both cases. Thus, it seems that CI internetwork peak formation resembles Ca II K<sub>2V</sub> internetwork peak formation sufficiently closely that the Carlsson & Stein simulations should be taken as interpretative guide.

### 4.3. Vertical patterning

The Ca II  $H_{2V}$  peaks in the Carlsson-Stein diagrams form at heights at which the shocks have just started to develop, have small strength, and are yet below the height of frequent shock overtaking. The  $H_{2V}$  grains therefore display fairly regular modulation in the simulated spectral evolution diagrams (Figs. 12–13 of Carlsson & Stein). Comparable CI line formation at larger height should not only suffer from much larger shock amplitudes, but also from much more confusion due to shock interference. Similarly, there should be less clear correlation with the intensity modulation in deeper layers. The Carlsson–Stein evolution diagrams display well-correlated behavior in the inner wings which closely reproduces the observed Ca II wing “whisker modulation” observed by Beckers & Artzner (1974). For a larger height separation between line-center formation and line-wing formation, the correlation will be less good.

Translation to the 160 nm diagnostics studied here implies that CI jets represent CI profile peaks that are comparable to  $K_{2V}$  peaks but are formed at larger height in the atmosphere, whereas the 160 nm brightness variation is comparable to the Ca II inner-wing whisker modulation. This seems a likely proposition. The large solar confusion that is apparent from our data should then result from the larger amount of interference variations between shocks at larger height. The large phase difference between CI Dopplershift modulation and 160 nm brightness modulation, larger than  $K_{2V}$ –whisker phase differences, may also result from the larger CI formation height. The differences between blue and red jets should arise similarly to the differences between  $K_{2V}$  and  $K_{2R}$  peaks. The actual gas motions are then only a fraction of the measured CI Dopplershifts, comparable to the factor two skewing in  $K_{2V}$  peak location.

### 4.4. Horizontal patterning

The observed horizontal scalings cannot be explained from the Carlsson-Stein simulations since the latter are one-dimensional. Our data confirm the split between two characteristic 160 nm scales observed by Foing & Bonnet (1984a, 1984b), Foing et al. (1986) and Cook & Ewing (1991) into mesoscale patches of 3–7 Mm and 1.4–3 Mm separation between bright points, as evident in Fig. 2 and Figs. 8–9. A similar split is seen for CI Dopplershift in Figs. 1 and 10.

The mesoscale patterning is also observed in Ca II  $K_{2V}$  from internetwork regions. It is presumably set by the internetwork three-minute waves and shock dynamics discussed above (Cram 1978; Cram & Damé 1983; Damé & Martić 1987; Lites et al. 1993; cf. Rutten

& Uitenbroek 1991a).

The small-scale patterning is puzzling. In a conference presentation of our data, Hoekzema (1994) speculated that the three-minute buffeting of a thermal interface or steep gradient between lower and upper internetwork chromosphere, possibly marking the magnetic canopy, excites horizontally spreading three-minute surface waves that cause the observed small-scale structuring. He suggested that the 1–2 Mm separations which bright points and CI jets favor in Figs. 8–10 are due to modulation by waves with  $f$ -mode character as studied theoretically by Campbell & Roberts (1989), Evans & Roberts (1990) and Rosenthal & Gough (1994). This spatial scale corresponds to  $f$ -mode wavelengths for periodicities near three minutes in the low chromosphere (1.2–1.6 Mm).

The internetwork shocks are bound to excite surface waves with three-minute periodicity along any discontinuity (such as a magnetic canopy). Adding their velocity amplitude to the vertical shock dynamics causes small-scale modulation of the mesoscale shock patterning. Extreme Dopplershifts may then arise from constructive interference, describing motions that are less supersonic as seen by the gas itself. In addition, such surface-wave modulation may also explain the observed small size of the jet centers, the steep amplitude drop around them, the apparent jet-center splitting, and it may also cause the observed black-near-blue areas within jets by confusing the solar CI profiles through destructive interference. The striking difference in morphology in the lower-left panel of Fig. 8 between fast and slow modulation decay may mark superpositions of crossing surface wave fronts, causing slender, elongated ridges of large velocity. The contrast between blue-jet and red-jet perimeter variability in the lower-right panel of Fig. 9 may be due to compression and rarefaction from destructive, respectively constructive, interference between the mesoscale and  $f$ -mode excursions. Finally, such interference may also cause the frequently string-like appearance of the 160 nm bright point patterning.

## 5. CONCLUSION

We have found oscillatory relationships between CI Dopplershift variations and 160 nm intensity variations in chromospheric internetwork areas that seem related to the acoustic shock dynamics causing Ca II  $K_{2V}$  grains. They indicate that CI “jets” and 160 nm “bright points” are not the isolated features that these names suggest, but rather the extremes of more ubiquitous oscillation patterns. The relations surface only after extensive spatial averaging, which indicates the presence of much solar variation in behavior, scales and phases. This increase in complexity over H&K behavior may be ascribed to larger variations in shock amplitudes and shock interference patterns at larger height. In addition,

there is evidence of horizontal three-minute modulation at 1–2 Mm wavelength for which localized surface waves with  $f$ -mode character seem a likely candidate.

We have taken advantage of the absence of seeing-caused spatial deformations in the HRTS data through our spatial averaging over specific pixel classes. In the meantime, the SUMER spectrometer onboard the SOHO mission has become available. It provides excellent opportunities to study internetwork dynamics with much longer duration and with better statistics than is possible from rocket instruments, in particular enabling temporal and spatial Fourier decomposition and more refined phase difference and coherency studies. SOHO observing programs with simultaneous groundbased Ca II  $K_{2V}$  imaging and spectrometry are presently underway.

With regard to interpretation, numerical simulation of dynamical CI line formation and phase relationships with 160 nm brightness in Carlsson–Stein fashion will be worthwhile. The CI lines and similar ultraviolet lines provide an important diagnostic step up from Ca II H&K, to chromospheric heights where shock dynamics fully dominates. Obvious targets for reproduction are the counterphase patterns in Figs. 6 and 7.

Finally, we wish to emphasize that our correlations only hold statistically, after extensive spatial averaging. Although jets and bright points are part of oscillatory phenomena which we attribute to acoustic shock dynamics, there is so much solar interference that direct feature-by-feature linkage as in Paper I is not a good strategy. Future studies of chromospheric internetwork dynamics, whether based on SUMER data or on numerical simulations, must recognize and disentangle this intrinsic solar variety.

N.M. Hoekzema’s research was supported by the Netherlands Foundation for Research in Astronomy (NFRA) with financial aid from the Netherlands Organization for Scientific Research (NWO). J.W. Cook’s work was supported by NASA under DPR W–14,541 and by the Office of Naval Research.

## References

- Beckers, J. M., Artzner, G. 1974, *Solar Phys.*, 37, 309
- Bonnet, R. M., Bruner, M., Acton, L. W., Brown, W. A., Decaudin, M., Foing, B. 1982, *A&A*, 111, 125
- Campbell, W. R., Roberts, B. 1989, *ApJ*, 338, 538
- Carlsson, M., Stein, R. F. 1994, in M. Carlsson (ed.), *Chromospheric Dynamics, Proc. Miniworkshop, Inst. Theor. Astrophys., Oslo*, p. 47
- Carlsson, M., Stein, R. F. 1995, *ApJ*, 440, L29
- Cook, J. W., Brueckner, G. E., Bartoe, J.-D. F. 1983, *ApJ*, 270, L89
- Cook, J. W., Ewing, J. A. 1991, *ApJ*, 371, 804
- Cook, J. W., Rutten, R. J., Hoekzema, N. M. 1996, *ApJ*, in press
- Cram, L. E. 1978, *A&A*, 70, 345
- Cram, L. E., Damé, L. 1983, *ApJ*, 272, 355
- Damé, L., Martić, M. 1987, *ApJ*, 314, L15
- Dere, K. P., Bartoe, J.-D. F., Brueckner, G. E. 1983, *ApJ*, 267, L65
- Dere, K. P., Bartoe, J.-D. F., Brueckner, G. E. 1986, *ApJ*, 305, 947
- Deubner, F.-L., Hoffmann, J., Kossack, E., Fleck, B. 1994, in R. J. Rutten, C. J. Schrijver (eds.), *Solar Surface Magnetism, NATO ASI Series C433, Kluwer, Dordrecht*, p. 155
- Evans, D. J., Roberts, B. 1990, *ApJ*, 356, 704
- Foing, B., Bonnet, R. M. 1984a, *A&A*, 136, 133
- Foing, B., Bonnet, R. M. 1984b, *ApJ*, 279, 848
- Foing, B., Bonnet, R.-M., Bruner, M. 1986, *A&A*, 162, 292
- Hoekzema, N. M. 1994, in M. Carlsson (ed.), *Chromospheric Dynamics, Proc. Miniworkshop, Inst. Theor. Astrophys., Oslo*, p. 111
- Hofmann, J., Steffens, S., Deubner, F.-L. 1995, *A&A*, 308, 192
- Lites, B. W., Rutten, R. J., Kalkofen, W. 1993, *ApJ*, 414, 345
- Martić, M., Damé, L. 1989, in R. J. Rutten, G. Severino (eds.), *Solar and Stellar*

- Granulation, NATO ASI Series C 263, Kluwer, Dordrecht, p. 207
- Martić, M., Damé, L., Bruner, M. E., Foing, B. H. 1991, *Adv. Space Res.*, 11, (5)241
- Rosenthal, C. S., Gough, D. O. 1994, *ApJ*, 423, 488
- Rutten, R. J. 1994, in M. Carlsson (ed.), *Chromospheric Dynamics*, Proc. Miniworkshop, Inst. Theor. Astrophys., Oslo, p. 25
- Rutten, R. J. 1995, in J. T. Hoeksema, V. Domingo, B. Fleck, B. Battrock (eds.), *Helioseismology*, Proc. Fourth SOHO Workshop, ESA SP-376 Vol. 1, ESA Publ. Div., ESTEC, Noordwijk, p. 151
- Rutten, R. J., Uitenbroek, H. 1991a, *Solar Phys.*, 134, 15
- Rutten, R. J., Uitenbroek, H. 1991b, in P. Ulmschneider, E. R. Priest, R. Rosner (eds.), *Mechanisms of Chromospheric and Coronal Heating*, Proc. Heidelberg Conf., Springer Verlag, Berlin, p. 48
- Shine, R. A., Lites, B. W., Chipman, E. G. 1978, *ApJ*, 224, 247
- Vernazza, J. E., Avrett, E. H., Loeser, R. 1981, *ApJS*, 45, 635

**Figure captions**

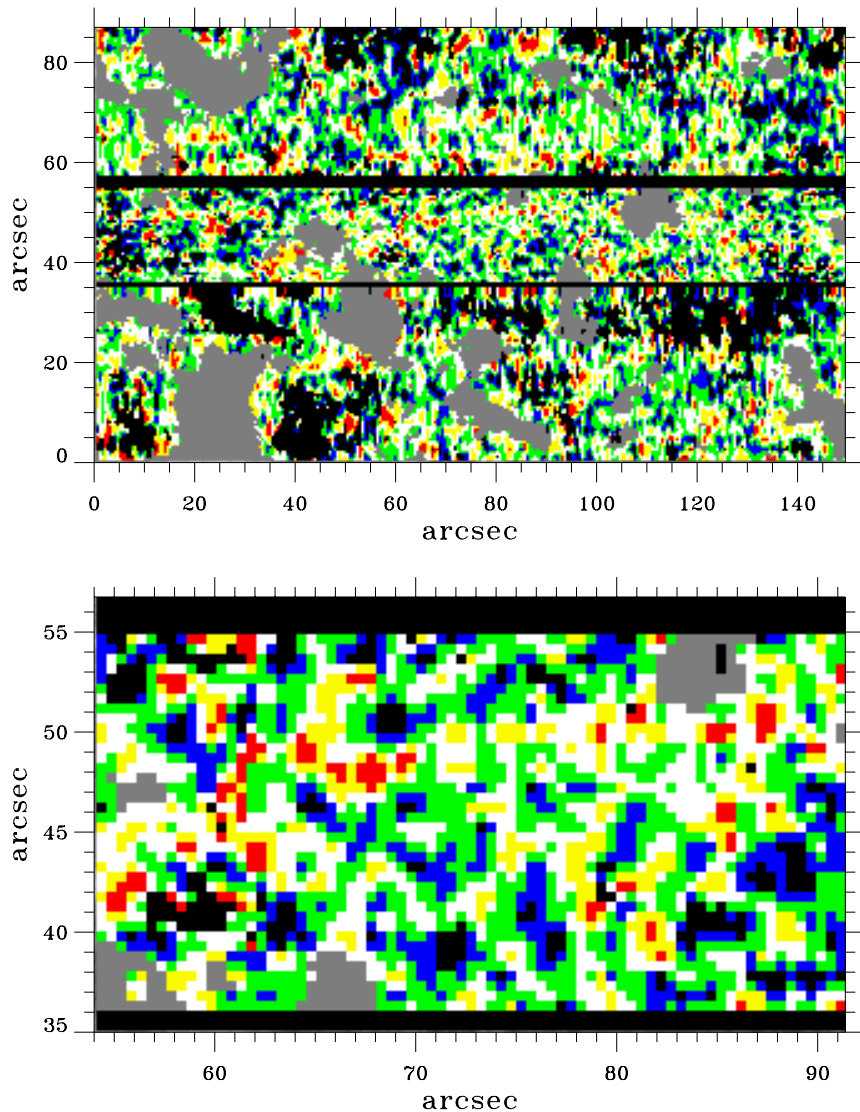


Fig. 1.— Upper panel: CI Dopplershift map for the  $150 \times 87$  arcsec subfield. Lower panel: blow-up of the center region. Dopplershift color coding, with blueshift (upward motion) positive: blue  $\Delta\lambda_D > 15 \text{ km s}^{-1}$  (“blue jets”), green  $5 < \Delta\lambda_D < 15 \text{ km s}^{-1}$ , white  $-5 < \Delta\lambda_D < 5 \text{ km s}^{-1}$ , yellow  $-15 < \Delta\lambda_D < -5 \text{ km s}^{-1}$ , red  $\Delta\lambda_D < -15 \text{ km s}^{-1}$  (“red jets”). The color grey marks blanked-out network areas that are not analyzed in this paper. Black defines areas without Dopplershift measurement. The horizontal black strips are data gaps at which the spectrograph scanning was changed. The field was scanned sequentially from bottom to top, with the 1 arcsec wide slit oriented horizontally. The lower and upper part were scanned in 2 arcsec vertical steps, the middle panel in 1 arcsec steps. The 0.5 arcsec map pixels result from interpolation between these scan steps; the coarser vertical sampling at the top and bottom produces stretched appearance. The remaining dark areas are locations where the measurement algorithm found no well-defined emission features (“black pixels”). The bottom panel magnifies a  $37 \times 21$  arcsec subfield located at the center of the upper panel, with corresponding axis coordinates. It was measured, bottom to top, from  $t = 263 \text{ s}$  to  $t = 311 \text{ s}$  after launch. It shows that blueshifts outweigh redshifts, that small black areas tend to reside within blue ones, and suggests the presence of both large-scale and small-scale modulation.

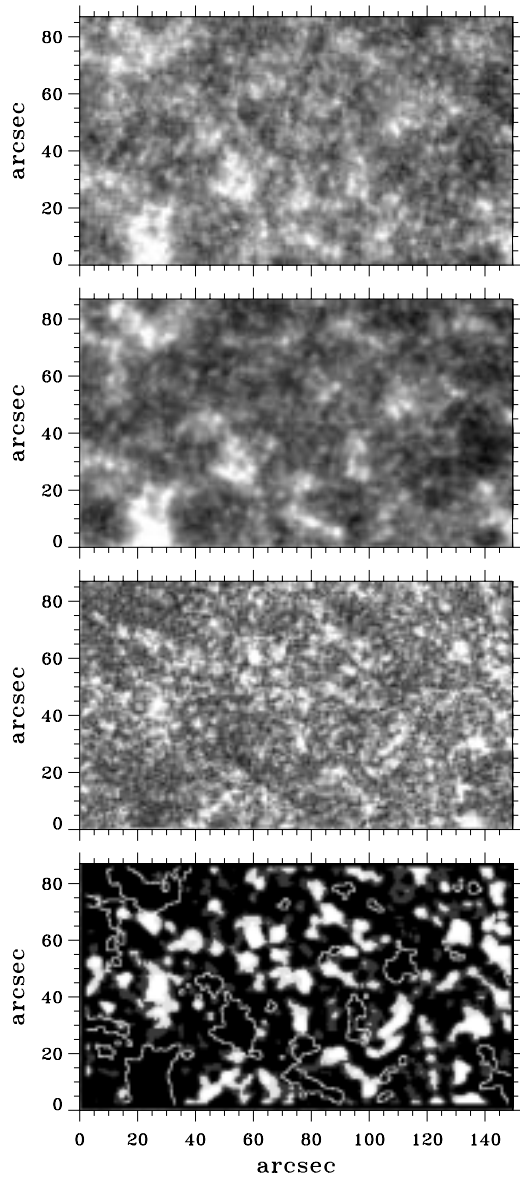


Fig. 2.— Four 160 nm brightness maps for the  $150 \times 87$  arcsec subfield. Top panel: the first of the seven heliograms, taken at  $t = 199$  s after launch. The chromospheric network stands out as large bright patches, while internetwork areas contain clusters of bright points of varying size and intensity. Second panel: temporal average of the seven heliograms, covering 160 s. The steady network pattern gains contrast while the short-lived internetwork bright points and noise from film graininess cancel out. Third panel: rms temporal brightness variation  $\sigma T_b$  per pixel over the seven heliograms. The network shows appreciably smaller temporal variability than the internetwork regions. The latter show much spatial variation in temporal variability, with clumpy patterning. Bottom panel: spatially smoothed rms brightness variation, using coarse brightness binning to emphasize meso-scale patterning. The overlaid contours outline the network mask used throughout the paper.

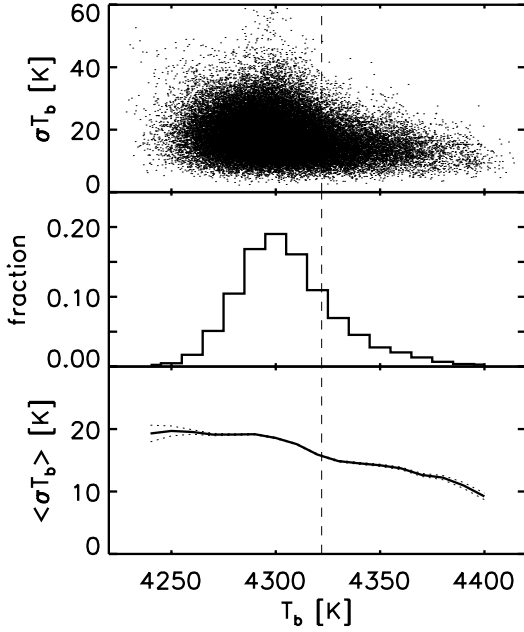


Fig. 3.— Brightness temperature variability  $\sigma T_b$  against time-averaged brightness temperature  $T_b$  per pixel. The dashed line defines the cutoff used to mask out the network (brighter). Upper panel: pixel-by-pixel scatter diagram. Middle panel: histogram of the pixel fraction per  $T_b$  bin. Bottom panel: bin averages on an expanded vertical scale, with one-sigma variances (dotted).

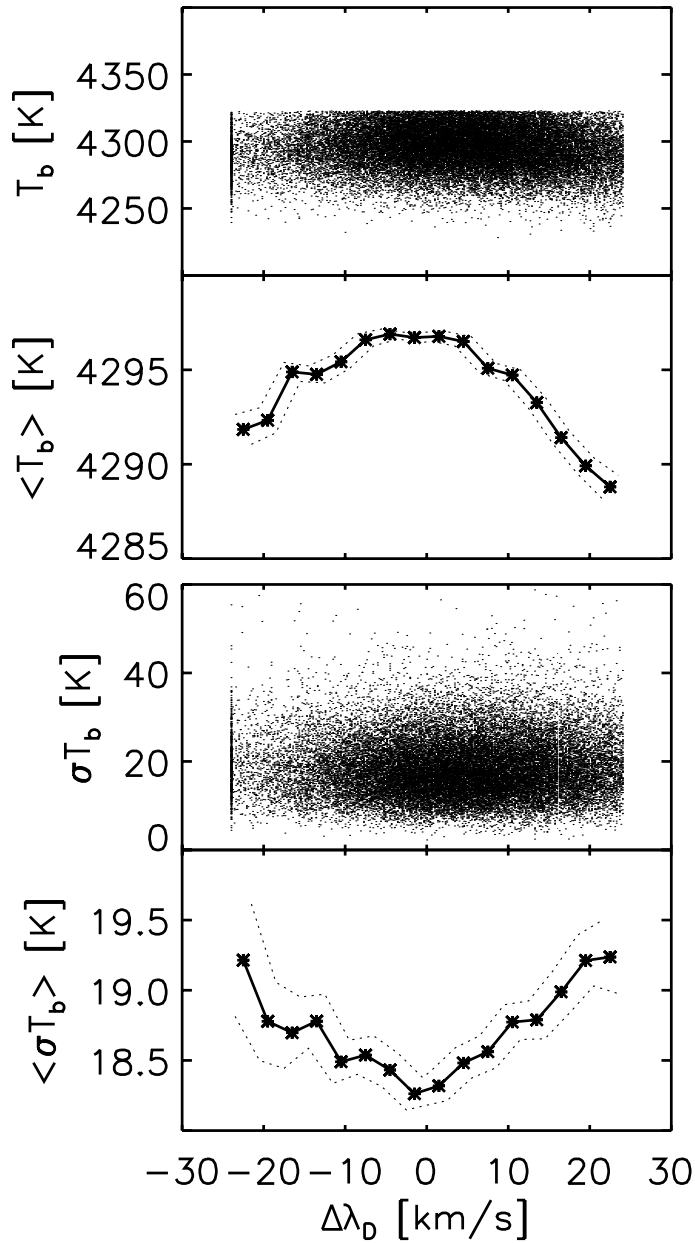


Fig. 4.— Statistical relations between brightness properties per pixel (vertical) and Dopplershift  $\Delta\lambda_D$  per pixel (horizontal). The upper graph is for time-averaged brightness temperature  $T_b$ ; the lower graph for temporal brightness variability  $\sigma T_b$ . The scatter plots in the upper panels are cut at  $\Delta\lambda_D = \pm 24 \text{ km s}^{-1}$  by the measurement algorithm; the upper scatter cutoff in the top panel is due to the exclusion of network pixels with  $T_b > 4322 \text{ K}$ . The lower panels show averages per  $3 \text{ km s}^{-1}$  Dopplershift bins, on much expanded vertical scales. The variances are standard deviations of the bin averages.

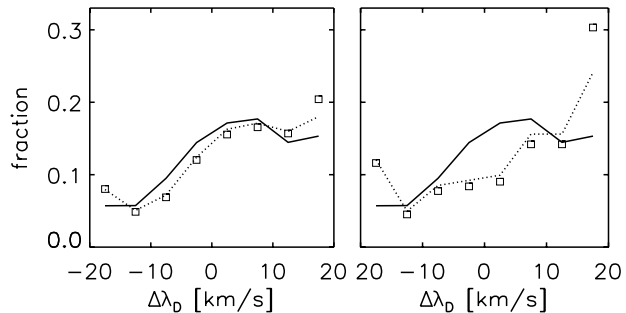


Fig. 5.— Bright point statistics. Solid: distribution over CI Dopplershift for all colored (non-black and non-grey) pixels in Fig. 1. Dotted: Dopplershift distributions for locations with large 160 nm brightness variability only. Left: locations with  $32 < \sigma T_b < 43$  K. Right: locations with  $\sigma T_b > 43$  K. The squares result when black pixels in Fig. 1 that are adjacent to blue jets are also included as blue jets.

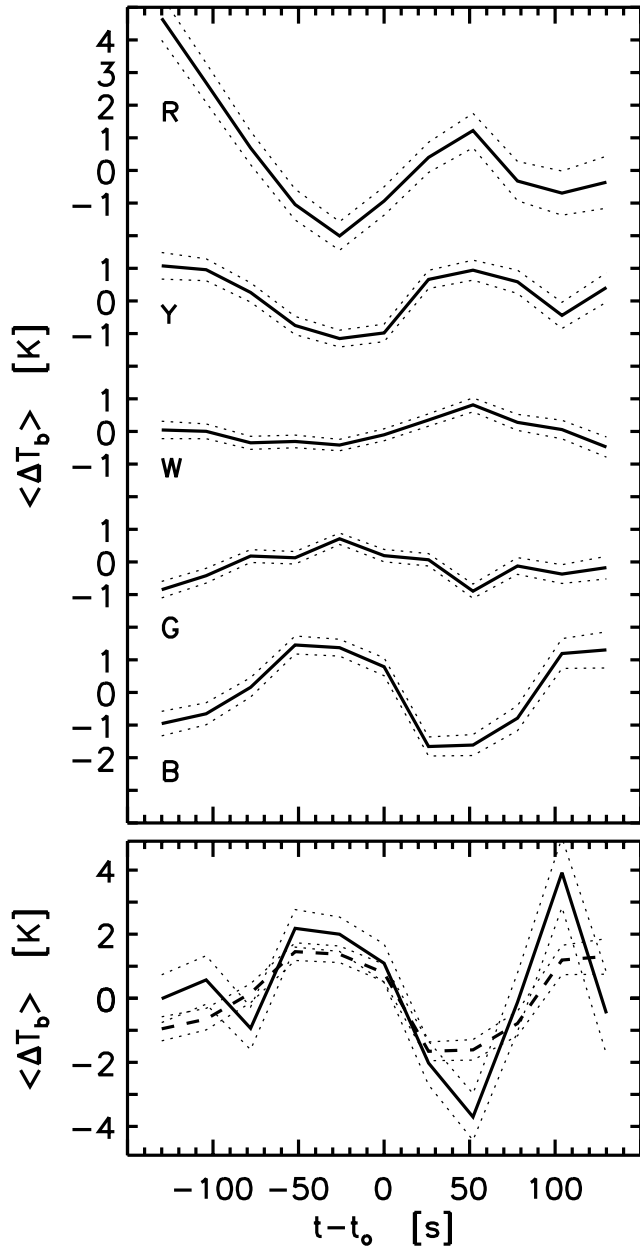


Fig. 6.— Time delay statistics. The abscissa measures the temporal separation  $t - t_0$  between the CI Dopplershift measurement of a pixel at time  $t = t_0$  and its brightness measurement from one of the seven 160 nm heliograms. Negative values imply brightness sampling before Dopplershift sampling. The ordinate is the corresponding difference between the instantaneous 160 nm brightness of a pixel and its time-averaged value, spatially averaged per time delay bin over all pixels per Dopplershift bin. The latter bins are coded by letters according to the color coding in Fig. 1. The dotted curves show the variances of the bin averages. A small-amplitude but significant brightness modulation appears, with three-minute periodicity and opposite phase between red jets (top curve) and blue jets (bottom curve). The lower panel is a similar plot for black pixels with a blue-jet neighborhood (solid curve). The blue-jet curve is added for comparison (dashed).

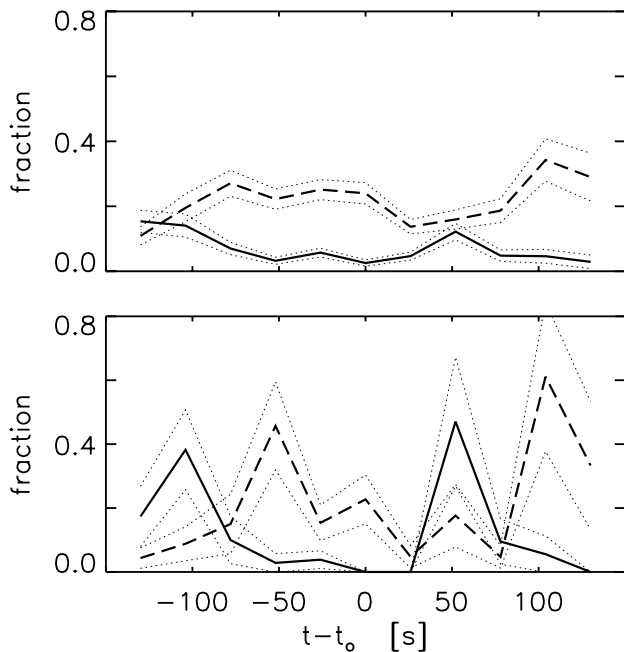


Fig. 7.— Time delay statistics for bright points only. Upper panel: bright points defined as internetwork pixels that at time  $t$  were  $45 < \Delta T_b < 60$  K brighter than their temporal mean. Lower panel: bright points defined as internetwork pixels that at time  $t$  were  $\Delta T_b > 60$  K brighter than their temporal mean. The abscissae again measure the temporal separation between 160 nm brightness sampling and CI Dopplershift sampling. The distributions measure the fraction of all such bright point pixels per time delay bin that coincide with a red jet at  $t = t_0$  (solid curves) or with a blue jet or black-near-blue pixel at  $t = t_0$  (dashed). Especially the extreme brightenings concentrate at specific lags prior to or after blue jets and red jets.

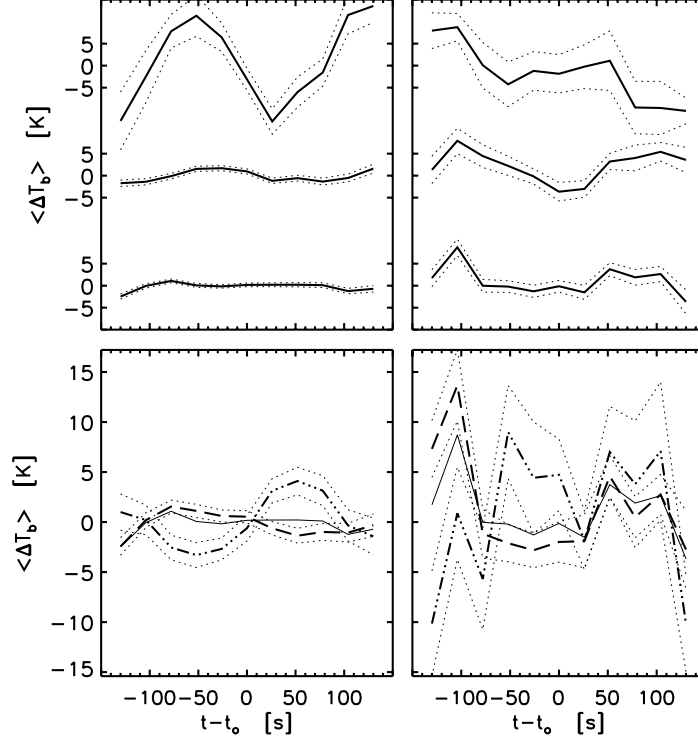


Fig. 8.— Time delay statistics as in Fig. 6, split for jet geometry. The abscissae again measure time delay between the Dopplershift sampling at  $t = t_0$  and the 160 nm brightness sampling. The ordinates again measure the instantaneous 160 nm brightness of a pixel minus its time average. However, the spatial averaging is now done over jet-geometry subclasses. The upper-left panel is for blue jets. The top curve is for their centers, the middle curve for the remaining blue-jet pixels, the bottom curve for blue-jet perimeters. The upper-right panel is similarly split for red jets. The bottom panels, also for blue jets (left) and red jets (right), split the spatial averaging over perimeter pixels between those with high Dopplershift (dashed,  $10 < |\Delta\lambda_D| < 15 \text{ km s}^{-1}$ ) and low Dopplershift (dot-dashed,  $0 < |\Delta\lambda_D| < 3 \text{ km s}^{-1}$ ). The thin solid curves are for all perimeter pixels (same as bottom curves in upper panels). The dotted curves show the variances of the averages. For blue jets the correlation between brightness modulation and Dopplershift drops off steeply away from jet center, with sign reversal for low-Dopplershift perimeters.

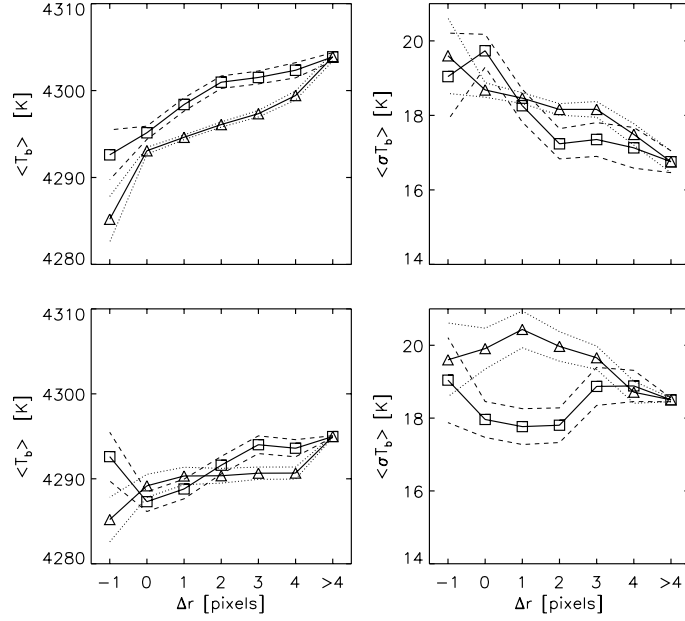


Fig. 9.— Statistical relations between CI Dopplershift and 160 nm brightness for blue jets (triangles) and red jets (squares). The abscissae measure the distance to jet center areas of successive pixel rings around jets, in pixel widths with  $\Delta r = -1$  denoting jet center pixels,  $\Delta r = 0$  the remaining jet pixels,  $\Delta r = 1$  jet perimeter pixels,  $\Delta r = 2 - 4$  pixels at that distance from a jet, and  $\Delta r > 4$  all remaining pixels. The lefthand panels measure mean pixel brightness temperature  $T_b$ , temporally averaged over the seven 160 nm heliograms and spatially averaged over all pixels per bin. The righthand panels measure temporal brightness variability per pixel, similarly averaged spatially. In the lower panels the spatial averaging is limited to only those jets that possess jet centers. The dotted curves are average variances. These plots suggest the presence of small-scale (3–4 pixel) spatial modulation.

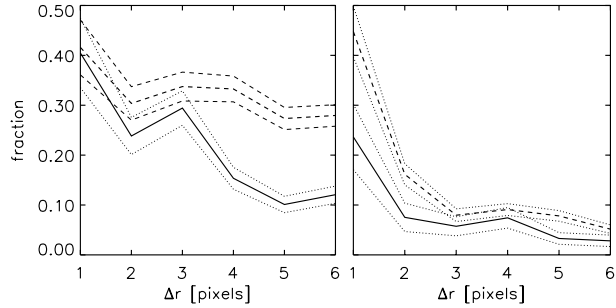


Fig. 10.— Jet separation statistics, respectively for blue jets (left) and red jets (right). For each type, well-separated jets were selected with  $|\Delta\lambda_{\text{D}}| \gg 24 \text{ km s}^{-1}$  (the outer limits in Fig. 4) within two subfields. The curves measure, for each field separately (solid and dashed), the surface fraction of the pixels around the jets with  $|\Delta\lambda_{\text{D}}| > 21 \text{ km s}^{-1}$  as a function of the distance to the jet. The variances are Poisson estimates. The humps suggest preference for 3–4 pixel separations between jets.